Crystal structure of a SNARE complex involved in synaptic exocytosis at 2.4 Å resolution

R. Bryan Sutton*, **Dirk Fasshauer**†, **Reinhard Jahn**† & **Axel T. Brunger***

* *The Howard Hughes Medical Institute and Department of Molecular Biophysics and Biochemistry, Yale University, New Haven, Connecticut 06520, USA*
† *Department of Neurobiology, Max-Planck-Institute for Biophysical Chemistry, D-37077 Göttingen, Germany*

....

The evolutionarily conserved SNARE proteins and their complexes are involved in the fusion of vesicles with their target membranes; however, the overall organization and structural details of these complexes are unknown. Here we report the X-ray crystal structure at 2.4 Å resolution of a core synaptic fusion complex containing syntaxin-1A, synaptobrevin-II and SNAP-25B. The structure reveals a highly twisted and parallel four-helix bundle that differs from the bundles described for the haemagglutinin and HIV/SIV gp41 membrane-fusion proteins. Conserved leucine-zipper-like layers are found at the centre of the synaptic fusion complex. Embedded within these leucine-zipper layers is an ionic layer consisting of an arginine and three glutamine residues contributed from each of the four α-helices. These residues are highly conserved across the entire SNARE family. The regions flanking the leucine-zipper-like layers contain a hydrophobic core similar to that of more general four-helix-bundle proteins. The surface of the synaptic fusion complex is highly grooved and possesses distinct hydrophilic, hydrophobic and charged regions. These characteristics may be important for membrane fusion and for the binding of regulatory factors affecting neurotransmission.

Fusion of a vesicle with its target membrane is mediated by a set of conserved proteins collectively referred to as SNAREs (soluble NSF-attachment protein (SNAP) receptors; NSF is *N*-ethylmaleimide-sensitive fusion protein)[1,2]. In exocytosis of synaptic vesicles, these SNAREs include the plasma-membrane-associated proteins syntaxin and SNAP-25 (synaptosome-associated protein of relative molecular mass 25K), and the vesicular protein synaptobrevin. Although the function of the SNAREs in membrane fusion is not fully understood, it must be fundamental because proteolytic cleavage of the SNAREs by clostridial neurotoxins inhibits neurotransmission[3]. SNARE proteins spontaneously assemble into a stable ternary complex that has a melting temperature (T_m) of 90 °C[4-6]. According to present theories, after the SNARE proteins form a complex, the vesicle and target membranes fuse, thereby releasing neurotransmitter into the synaptic cleft[2]. After fusion, the SNARE complex can then recruit a member of the SNAP family[7,8]. Addition of SNAPs to the SNARE complex allows binding of NSF, an ATPase that catalyses the dissociation of the ternary SNARE complex, thereby priming the SNAREs for another round of fusion[4,5,9,10].

Because the assembly of synaptic SNAREs is important in mediating neurotransmission, information about the SNARE-complex structure is crucial to understanding the detailed interactions among SNAREs and with other regulatory factors. Here we report the 2.4 Å crystal structure of the synaptic fusion complex consisting of the cytoplasmic domain of synaptobrevin-II, the carboxy-terminal H3 domain of syntaxin-1A, and the amino- and carboxy-terminal domains of SNAP-25B (ref. 11). We have shown previously that this core complex resembles the full-length complex with respect to assembly, disassembly, and biophysical properties[6,11].

Structure determination

The core synaptic fusion complex was obtained by limited proteolysis, mass-spectrometry analysis, and bacterial expression of the fragments[11]. The complex consists of syntaxin-1A residues Gly 180–Arg 262 (Sx), synaptobrevin-II residues Met 1–Met 96 (Sb), and the

Table 1 Crystallographic data, phasing and refinement

Crystal*	a (Å)	b (Å)	c (Å)	λ (Å)	d_{min} (Å)	Observed reflections (n)	Unique reflections (n)	Completeness (%)	$\langle I \rangle / \langle \sigma_I \rangle$	R_{sym}† (%)
Native	100.54	112.71	200.77	1.0332	2.4	309,408	42,980	99.1 (98.8)	17.4	7.9 (32.9)
Iodine	100.44	112.77	199.00	1.0332	3.0	81,645	42,094	96.2 (89.1)	12.0	6.7 (46.2)
SeMetSn1	98.72	111.07	198.84	0.9797	3.0	160,622	46,665	99.7 (99.4)	17.0	8.1 (37.7)
SeMetSx	100.11	113.13	198.93							
λ₁ (low-energy remote)				1.0688	3.2	120,963	25,261	97.9 (97.9)	16.9	6.4 (26.9)
λ₂ (inflection point)				0.9801	3.2	110,188	35,008	97.3 (95.9)	13.0	7.9 (32.0)
λ₃ (anomalous peak)				0.9797	3.2	112,147	35,072	97.3 (96.1)	13.9	7.3 (32.0)
SeMetSn1Sn2	99.88	112.95	198.64							
λ₁ (low-energy remote)				1.0688	3.0	137,029	42,024	96.5 (86.3)	16.7	6.0 (28.3)
λ₂ (inflection point)				0.9800	3.0	129,455	41,257	95.1 (82.2)	13.8	7.2 (38.5)
λ₃ (anomalous peak)				0.9795	3.0	129,052	41,449	95.0 (81.6)	12.6	7.5 (42.0)
SeMetSn1Sn2	99.94	112.79	198.61							
λ₁ (low-energy remote)				1.0688	3.3	115,718	31,945	97.8 (98.5)	14.7	8.1 (28.3)
λ₂ (inflection point)				0.9800	3.3	113,142	31,613	97.3 (97.9)	13.8	10.4 (35.3)
λ₃ (anomalous peak)				0.9795	3.3	111,867	31,456	97.4 (97.7)	11.3	10.8 (38.0)

* Sn1Sn2, synaptic fusion complex with selenomethionine (SeMet) labels on both Sn1 and Sn2; Sn1SnSx, synaptic fusion complex with SeMet labels on Sn1, Sn2 and Sx. Values in parentheses are for the highest resolution bins.
† $R_{sym} = \Sigma_h \Sigma_i |I_i(h) - \langle I(h) \rangle| / \Sigma_h \langle I(h) \rangle$, where $I_i(h)$ is the *i*th measurement and $\langle I(h) \rangle$ is the weighted mean of all measurements of $I(h)$ for Miller indices *h*.

N- and C-terminal fragments of SNAP-25B, residues Met 1–Lys 83 (Sn1) and residues Val 120–Gly 206 (Sn2), respectively. We obtained crystals that exhibited limited diffraction, variable crystal quality, and high mosaicity. Cryotechniques combined with crystal annealing against increasing methylpentanediol (MPD) concentrations were essential in obtaining useful diffraction to a minimum Bragg spacing of 2.4 Å (Table 1). The crystals are of space group $I222$ ($a = 100.54$ Å, $b = 112.71$ Å, $c = 200.77$ Å; Table 1), with three synaptic fusion complexes and 54.8% solvent in the crystallographic asymmetric unit.

The complex was solved by a generalization of the method of multiwavelength anomalous dispersion (MAD) phasing[12]. Because of the size of the asymmetric unit and the limited crystal quality, multiple MAD experiments were required, each using a different combination of native and selenomethionine-labelled SNARE complexes (Table 1). Combination of the phases of the individual MAD experiments resulted in a significantly improved experimental electron-density map, because the directions of the heavy-atom structure factors are different for each combination of selenomethionine labels (Fig. 1 and Table 1 in Supplementary Information). Furthermore, the distribution of syntaxin-1A selenomethionine labels in one of the data sets allowed determination of the labelled methionine positions using an automated Patterson search method. The remaining sites were found by difference Fourier techniques. This 'multi-MAD' technique could be generally useful for structure solution of large macromolecular complexes with limited crystal quality and variability.

High-quality experimental phases allowed unbiased comparison of the three independent synaptic fusion complexes in the asymmetric unit. Of the three complexes, two are related by an approx-imate two-fold operation and the third complex is related by improper symmetry. These associations are mediated by ordered strontium ions and intercomplex sidechain interactions. Two strontium ions bridge the C termini of the synaptobrevin components of two antiparallel complexes. Another strontium ion bridges the syntaxin components of the two parallel orientated complexes. Although the synaptic fusion complex exhibits monomer–trimer equilibrium in solution[11], it is unknown whether these cation-mediated associations are related to any physiological function.

Overall topology

The synaptic fusion complex is arranged as a cylinder, 120 Å in length with circular cross-section (Fig. 2a). All four components of the heterotrimer are arranged in parallel, with the N termini at one end of the bundle and the C termini at the membrane-anchor end. The extreme N terminus of the core complex consists of a two-helix interaction between syntaxin and the Sn1 α-helix of SNAP-25. The central portion consists of a four-helix bundle with a left-handed superhelical pitch in which the synaptobrevin α-helix juxtaposes the syntaxin and Sn2 α-helices. The complex ends with a two-helix interaction between synaptobrevin and syntaxin at the C terminus.

The parallel orientation of synaptobrevin and syntaxin in the synaptic fusion complex has been shown by electron microscopy analysis[13]. However, parallel orientation of the two SNAP-25B α-helices was unexpected. In the full-length primary structure of SNAP-25B, a linker of 37 residues connects the Sn1 and Sn2 fragments. In the crystal structure, the N-terminal end of the Sn2 α-helix begins with a turn at residue Val 37, leaving 54 residues available to form a loop between the two SNAP-25 α-helices. This loop is probably palmitoylated *in vivo* at conserved cysteine residues
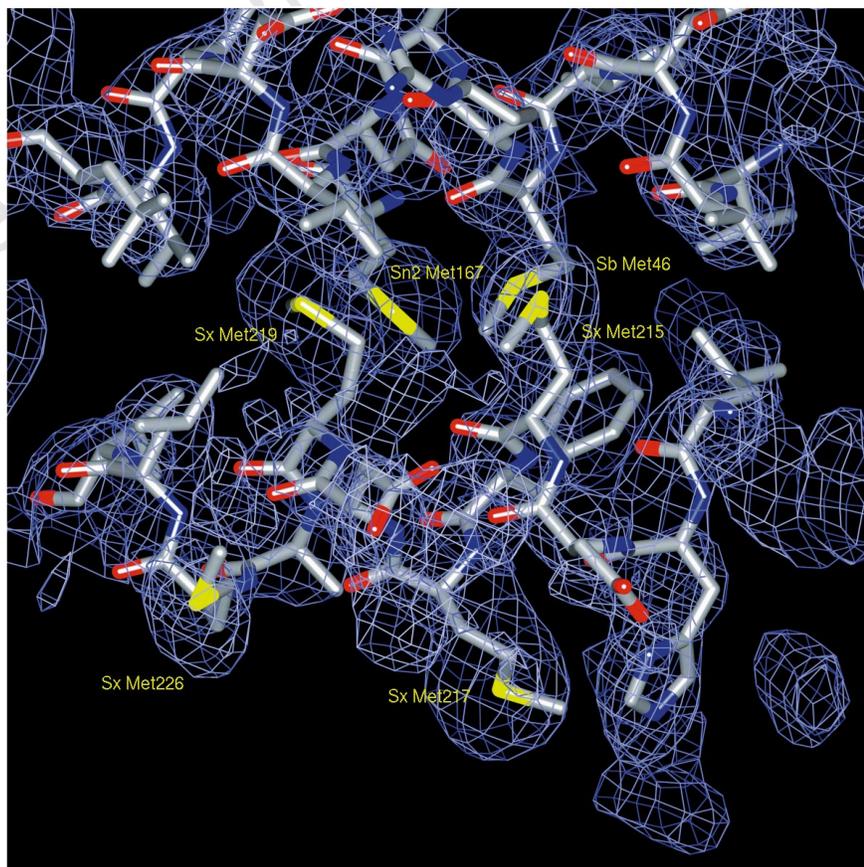

Figure 1 Electron-density map of the synaptic fusion complex obtained by multi-MAD phasing, showing a methionine cluster. Multi-MAD phases were obtained from phase combination of the Sx, Sn1Sn2 and Sn1Sn2Sx MAD data sets at 3 Å resolution, followed by density modification and phase extension to 2.4 Å resolution. The map was contoured at 1σ. The structure was superimposed as liquorice bonds.

and used as a membrane anchor[14]. As it is easily cleaved by proteases, the loop between SNAP-25 α-helices may be unstructured. We were concerned that, in the proteolytically cleaved synaptic complex, the SNAP-25B fragments might orientate themselves in the SNARE complex independently of each other, as the fragments are unrestrained. The parallel orientation of the Sn1 and Sn2 α-helices was shown by the location of the selenomethionine labels and by fitting the Sn1 and Sn2 structures to the experimental electron-density map. In addition, all of the Sn1 and Sn2 α-helices observed in the asymmetric unit possess the same parallel orientation. If there were a mixture of orientations in solution, one might expect the asymmetric unit in the crystal to reflect that distribution. Modelling of the entire SNAP-25B protein confirmed that the 54-residue loop between the two SNAP-25 α-helices was sufficient to span the 84 Å connecting the two fragments, thereby allowing a parallel orientation of α-helices.

Four-helix-bundle structure

Each of the three synaptic fusion complexes in the asymmetric unit possesses a different superhelical bend (Fig. 2b). We observed significant flexibility for both backbone and side-chain atoms in each of the molecules in the asymmetric unit (Fig. 2b). The overall pitch of the four-helix bundle is not defined, as each of the components in the bundle possesses its own unique α-helical character (Fig. 2c). The radius of the four-helix bundle changes significantly over the length of the bundle (Fig. 2d). The variation in the radius is correlated with sidechain packing in the core of the complex: the layers with the largest sidechain-packing volume show the largest radius.

Although the backbone topology of the complex (Fig. 2a) superficially resembles the tetrameric GCN4 four-helix-bundle structure[15], several factors differentiate the synaptic fusion complex from the leucine-zipper or coiled-coil proteins described so far. First, the distribution of leucine, isoleucine and valine residues as core constituents is not uniform over the length of the synaptic fusion complex. The composition of many layers includes residues other than leucine, isoleucine and valine residues (Table 2 in Supplementary Information), contrasting with typical leucine zipper proteins[16]. Second, the geometry of most of the layers in the synaptic fusion complex deviates significantly from that seen in the centre of the GCN4 tetramer structure (Table 2 in Supplementary Information). The leucine-zipper geometry, as found in the tetrameric GCN4 structure, derives from a generalization of Crick's classical coiled-coil model[17] to four-helix bundles. This model has planar and symmetrical layers whose normal is perpendicular to the superhelical bundle axis. Several regions in the individual proteins of the synaptic fusion complex are predicted to form a coiled-coil structure as they show heptad-repeat patterns (we used the Multi-Coil program[18]). These regions are from Leu 60 to Trp 90 of synaptobrevin-II, from Ala 5 to Arg 30 and from Leu 50 to Asp 80 of Sn1, and from Asn 169 to Gly 204 of Sn2. These patterns do not necessarily translate into a coiled-coil geometry for the entire four-helix bundle as the heptad-repeat patterns for the four individual fragments are not in register. As a consequence of these deviations
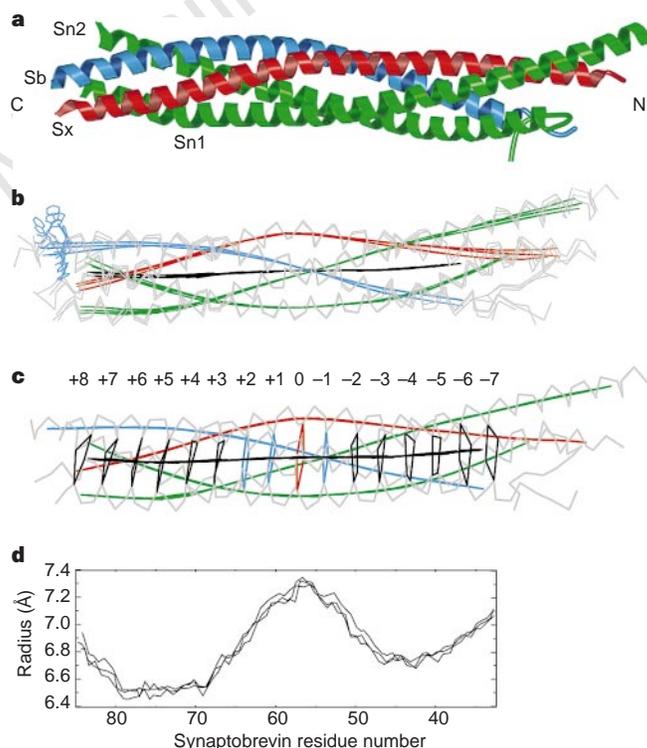

Figure 2 Topology and organization of the synaptic fusion complex. **a**, Backbone ribbon drawing of the synaptic fusion complex: blue, synaptobrevin-II; red, syntaxin-1A; green, SNAP-25B (Sn1 and Sn2). **b**, Conformational variability assessed by overlay of the three non-crystallographically related complexes. The backbones of layers −1, 0, +1 and +2 were superimposed with a pairwise r.m.s.d. of 0.3 Å. The N and C termini of the synaptic fusion complex show significant variation among complexes (maximum r.m.s.d. around the mean position for backbone atoms is 1.7 Å) and among side chains, such as Tyr 88, Trp 89, and Trp 90 in synaptobrevin (blue). C α traces are in grey. **c**, Organization of

the synaptic fusion complex. C α traces (grey), local helical axes (blue, red and green for synaptobrevin-II, syntaxin-1A and SNAP-25B, respectively), the super-helical axis (black), and layers (0, red; −1, +1 and +2, blue; all others black; numbers refer to Table 2 in Supplementary Information) are shown for one of the three complexes in the asymmetric unit. Layers are indicated by virtual bonds between corresponding C α positions. **d**, Radii of the three synaptic fusion complexes in the asymmetric unit. The radius is defined as the average distance between the local helical axes and the central four-helix-bundle axis.

from standard coiled-coil heptad-repeat pattern and geometry, the α-helical curvature is unique for each of the four components (Fig. 2a). The angle at which each α-helix crosses the overall bundle axis, or the crossing angle, ranges from a minimum of about 5° in syntaxin and Sn1 to as much as 25° in synaptobrevin and Sn2. Crick[17] predicted a crossing angle of 18° for dimeric coiled-coil proteins.

Residues from the four associating α-helices can be grouped into layers that are conserved in primary-structure alignments[19] and which are sensitive to mutations[20–23] (Fig. 2c). Layers ' − 1', '+1' and '+2' at the centre of the complex most closely follow ideal leucine-zipper geometry and amino-acid composition (Table 2 in Supplementary Information); each hydrophobic residue interacts in a plane. The layers are composed of leucine, isoleucine and valine residues and follow the packing characteristics of parallel, tetrameric leucine-zipper proteins[15]. However, in contrast to classical coiled-coil geometry, the tilt angles of the layers are between 8° and 14° with respect to the bundle axis (Fig. 2c, and Table 2 in Supplementary Information). Packing in the flanking regions of the central layers is typical of the more general class of α-helix-bundle proteins, as illustrated by the methionine cluster in Fig. 1.

Within the leucine-zipper layers, there is a highly conserved and completely buried '0' layer composed of Arg 56 from synaptobrevin-II, Gln 226 from syntaxin-1A, Gln 53 from Sn1 and Gln 174 from Sn2 (Fig. 3). The positively charged guanidino groups of the arginine residue interact with carboxyl groups from each of the three glutamine residues. The flanking leucine-zipper layers act as a water-tight seal to shield the ionic interactions from the surrounding solvent. This seal may further stabilize the four-helical oligomeric state and register of the complex by decreasing the local dielectric, thereby enhancing electrostatic interaction within the ionic layer. If another protein such as α-SNAP or NSF were able to puncture this seal, the ionic layer would be exposed to solvent, thereby increasing the local dielectric and weakening the interhelix interactions. This process may facilitate disassembly of the complex.

Surface structure

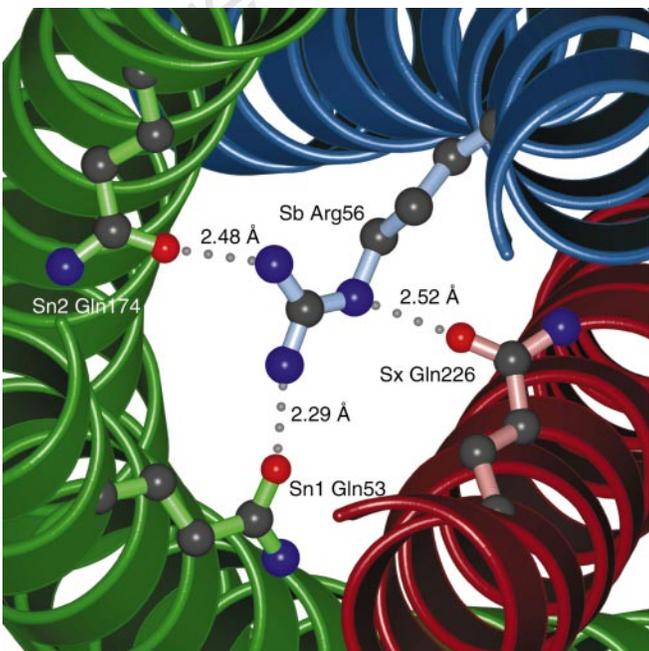There are four shallow grooves on the surface of the synaptic fusion complex, formed by the association of the α-helices. In a manner similar to the interaction of transcription factors with DNA, effectors such as α-SNAP or complexin could use the grooves of the synaptic fusion complex as specific binding sites, possibly forming a higher-order helical bundle. Indeed, the N-terminal end of Sn2 fold back and interacts through hydrophobic contacts to one of the grooves of the four-helix bundle formed by the vesicle (v)-SNARE, synaptobrevin and the Sn2 α-helix of the target membrane (t)-SNARE, SNAP-25B (Fig. 4).

The arrangement of the t-SNARE components syntaxin, Sn1 and Sn2 in the four-helix bundle allows formation of a cradle into which the v-SNARE, synaptobrevin, may bind. In the synaptic fusion complex, the α-helices are knitted together by hydrophobic interactions in the core as well by several disperse hydrogen-bonding or salt-bridging sidechain interactions on the solvent-exposed surface. Analysis of these surface interactions shows that there are significantly fewer interactions originating from the v-SNARE than those originating from each of the t-SNAREs. There are only two side chains that form strong salt-bridge interactions from synaptobrevin to syntaxin. There are five such interactions between synaptobrevin and the neighbouring Sn2 α-helix. This indicates that most of the binding energy for synaptobrevin in the synaptic fusion complex comes from hydrophobic and ionic core packing interactions. The t-SNAREs, however, maintain 17 surface salt bridges between each other, 10 formed between the SNAP-25B components and 7 of which are between syntaxin and its adjoining SNAP-25B α-helix (Sn1). Most of these ionic interactions are between the 'e' and 'g' positions of the heptad-repeat scheme. These observations may explain why binary complexes containing syntaxin-1A and SNAP-25B are more stable than binary complexes containing synaptobrevin and either syntaxin-1A or SNAP-25B (ref. 11).

Neurotoxin cleavage

The SNARE proteins are the targets for the clostridial neurotoxins, including botulinum and tetanus neurotoxins[3]. All

Figure 3 Ionic '0' layer of the synaptic fusion complex. Side chains involved in the layer are shown as balls and sticks; backbone is shown as a ribbon. The total buried surface area for the sidechain atoms in this layer is 742 Å.
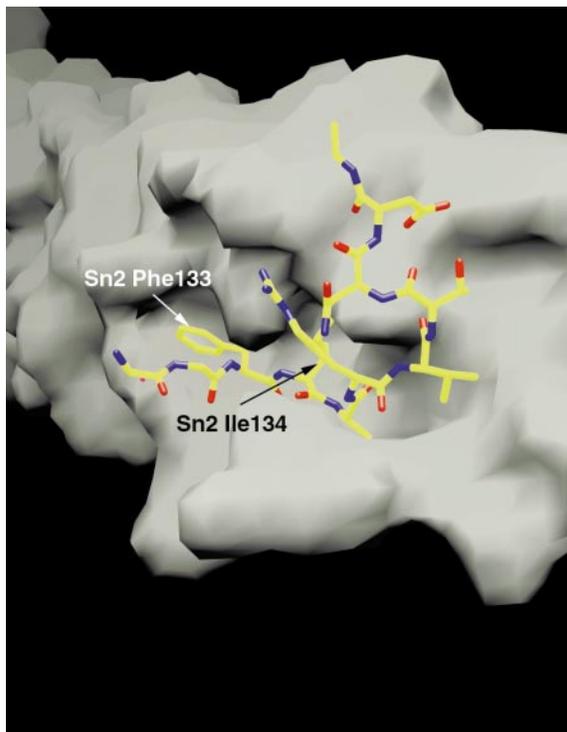

Figure 4 Close-up view of the loop involving Sn2 at the C-terminal end of the synaptic fusion complex. The SN2 loop continues as an extended peptide chain (shown as liquorice bonds) interacting with a hydrophobic groove in the synaptic fusion complex (shown as a molecular surface) formed by synaptobrevin and Sn2. Figure prepared with GRASP[48].
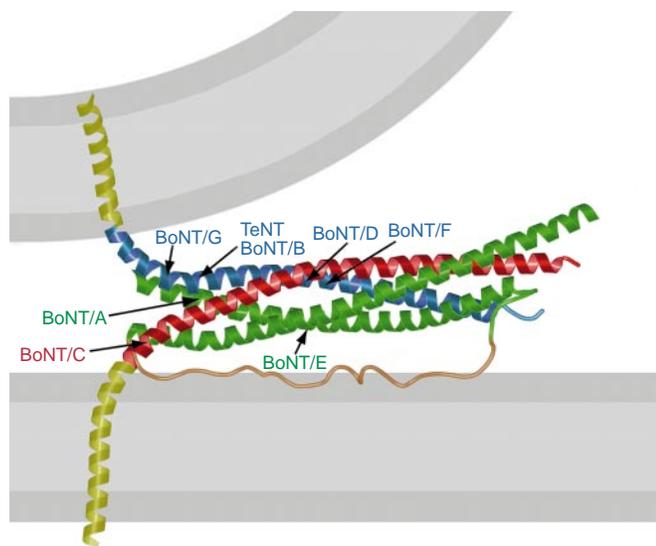
Figure 5 Hypothetical model of the synaptic fusion complex as it joins two membranes, and location of neurotoxin-mediated cleavage sites. We extended the synaptic fusion complex crystal structure to include the transmembrane domains (yellow) of syntaxin-1A (red) and synaptobrevin-II (blue), and the loop connecting the Sn1 and Sn2 fragments (green). The transmembrane domains and the linker to the Sx fragment are represented as α-helices. Hypothetical bends of the syntaxin and synaptobrevin α-helices were modelled close to the lipid bilayers. The loop between the Sn1 and Sn2 fragments was modelled as an unstructured polypeptide chain. The conformation of this loop is speculative. The loop between the Sn1 and Sn2 domains is shown in orange. We assumed that the lipid bilayers (grey) have a thickness of roughly 30 Å. The synaptobrevin-II neurotoxin-mediated cleavage site for tetanus toxin (TeNT) and botulinum toxin (BoNT) type B (BoNT/B) is between Gln 76 and Phe 77; for BoNT/F, between Gln 58 and Lys 59; for BoNT/G, between Ala 81 and Ala 82; and for BoNT/D, between Lys 59 and Leu 60. The syntaxin-1A BoNT/C cleavage site is between Lys 253 and Ala 254. Cleavage sites in SNAP-25B are between Asp 193 and Glu 194 for BoNT/E, and between Arg 176 and Gln 177 for BoNT/A.

neurotoxin-mediated cleavage sites are located between the C-terminal membrane anchors and the ionic '0' layer (Fig. 5). Only uncomplexed or partially assembled SNARE proteins can undergo proteolysis by neurotoxins[24]. The fully assembled SNARE complex is resistant to proteolysis because either the protease-cleavage sites or the protease-recognition sites are protected upon complex formation. An intermediate, partially assembled state may exist *in vivo* before fusion; in this complex the α-helices at C-terminal end are separated (Fig. 5). As neurotoxins cleave synaptobrevin and syntaxin close to the membrane, cleavage may detach either the presynaptic membrane or the vesicle membrane from the prefusion complex. In contrast, the result of cleavage of Sn2 by the botulinum neurotoxins, type A or E, is less direct as the C terminus of Sn2 is not directly anchored to the membrane. Cleavage by these toxins may destabilize the four-helical bundle of the synaptic fusion complex in the C-terminal region[24], and may disrupt the ability of the complex to join membranes.

Mechanistic implications for fusion

The assembly of the synaptic fusion complex probably begins with the formation of the binary complex, consisting of SNAP-25 and syntaxin, on the target membrane. After binding of synaptobrevin to the binary complex, the membrane anchors of syntaxin and synaptobrevin are positioned on the same side of the complex (Fig. 5). Electrostatic calculations show a pronounced basic-charge distribution at the membrane-anchored end, or C terminus, of the synaptic fusion complex (Fig. 6). When the four α-helices coalesce
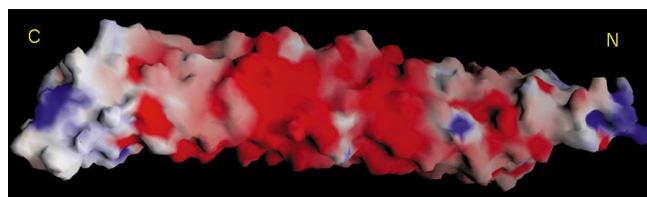

Figure 6 Surface plot showing the electrostatic potential of the synaptic fusion complex. Blue, positive charge; red, negative charge. Charges were obtained from the OPLS force field[50]. The electrostatic surface was contoured between − 10 kT/e and +10 kT/e. Figure prepared with GRASP[48].

into a complex immediately before fusion, the cumulative electrostatic potential may promote membrane fusion by affecting both membrane surfaces. Two tryptophan residues and a tyrosine are exposed to solvent at the C terminus of synaptobrevin-II in the crystal structure (Fig. 2b). These residues may associate with the membrane interface, as is often found in other membrane proteins[25], and may help in the fusion of vesicle and target membranes.

The inherent flexibility of the synaptic fusion complex may also contribute to its membrane-fusion activity. The predicted 20-residue transmembrane domain of synaptobrevin-II begins immediately at the C-terminal end of the Sb fragment. Likewise, the 23-residue transmembrane domain of syntaxin-1A and a 5-residue basic linker precede the Sx fragment. The transmembrane domains of syntaxin and synaptobrevin are probably α-helical, as the number of hydrophobic residues in the transmembrane domains would be sufficient to form a bilayer-spanning α-helix (Fig. 5). It is possible that the transmembrane α-helices would continue into the α-helices found in the synaptic fusion complex. If the synaptic fusion complex is involved in joining vesicles and target membranes, one would expect significant distortion or bending of the α-helices (Fig. 5). Indeed, flexibility of the α-helices is observed in both C-terminal and N-terminal regions (Fig. 2b). According to this model, the strain introduced by the α-helices may deform the lipid bilayers and promote lipid mixing.

The synaptic fusion complex is unlike the homo-oligomeric α-helical bundles that are found in the HIV/SIV gp41 (refs 26–28, 51) and the influenza virus haemagglutinin[29] crystal structures. These viral proteins may also be involved in promoting membrane fusion by a conformational change and subsequent antiparallel association of α-helices. In contrast, the synaptic fusion complex is a heterotrimeric, parallel four-helix bundle. The individual protein components of the synaptic fusion complex show little tendency to oligomerize, unlike the viral fusion proteins[6,30]. This preference for heterotrimerization is determined by packing interactions in the core, flanking ionic side-chain interactions on the surface of the fusion complex, and the interactions in the ionic '0' layer. A common theme among recent models of fusion is emerging, namely the joining of two membrane surfaces through a proteinaceous agent. In the case of viral fusion, conformational changes in the fusion protein accomplish the juxtaposition of membranes[31], whereas in the synaptic fusion complex, the assembly of the heterotrimer itself leads to fusion (Fig. 5). It remains to be determined whether the free energy released by the assembly of the synaptic fusion complex is sufficient to induce lipid mixing. Perhaps this process is assisted or regulated by accessory proteins, which could link Ca^{2+}-dependent exocytosis and the synaptic fusion complex. □

Methods

Protein production, crystallization and data collection. Characterization of the core synaptic fusion complex is described elsewhere[11]. The four fusion-complex components were cloned into vector pET-28b (Novagen) and grown

in BL21(DE3) *Escherichia coli* cells (Novagen) with 50 mg ml^{-1} kanamycin in a 10-l BioFlo3000 fermentor (New Brunswick Scientific) using enriched high-density media[32] for Sb and defined media for the Sx, Sn1 and Sn2 components (T. J. Griffin, personal communication). Cells were induced with 0.8 mM isopropylthiogalactoside (IPTG) at an $A_{600} = 20.0$–40.0, collected by centrifugation, and flash-frozen in liquid nitrogen. Purification followed the previously published protocol[11]. The iodine derivative was prepared by incubating Sb in 10 mM sodium iodide followed by addition of iodo-beads (Pierce) before complex formation. Selenomethionine-labelled proteins were obtained by expression in the B834λ(DE3) (Novagen) auxotroph, grown to $A_{600} = 2.0$–3.0 in selenomethionine-containing defined media[33], and purified in the presence of 10 mM dithiothreitol (DTT). Composition of the purified complex, iodine and selenomethionine incorporation were assessed by MALDI-TOF mass spectrometry (Perseptive).

Crystals of the complex were obtained by vapour diffusion at 29 °C using the sitting droplet method with microbridges (Hampton) placed inside multiwell VDX crystallization plates (Hampton) together with 1 ml reservoir solution and 10 μl top solution. The reservoir solution contained 35% MPD (*v/v*), 5% PEG 350 monomethylether (MME) (*v/v*), 25 mM Tris-HCl, pH 7.0, 70 mM SrCl$_2$ and 250 mM urea. The top solution contained 24.5% MPD (*v/v*), 3.5% PEG350 (MME) (*v/v*), 17.5 mM Tris, pH 7.0, 49 mM SrCl$_2$, 175 mM urea, 3.75 mM Sarkosyl and 10 mg ml^{-1} protein. Typically, small diamond-shaped crystals appeared overnight and continued to grow to a maximum size of 0.4 mm in the longest dimension within one week. Crystals were cryoprotected by transferring into increasing amounts of MPD, from an initial solution of 55% MPD, 25 mM SrCl$_2$ and 10 mM Tris, pH 7.0, to a final concentration of 75% MPD. Crystals typically cracked at 65–70% MPD, but reannealed over the course of 30 min. 20 mM DTT was included in the crystallization and cryoprotection solution of the selenomethionine crystals. Cryoprotected crystals were frozen in propane before data collection. Crystals were mosaic (around 1.5°) and showed variability in cell dimensions and diffraction quality (Table 1).

Diffraction data of the native, the selenomethionine-labelled Sn1, and iodine derivatives were collected at beamline 19ID at APS using an in-house CCD detector. The derivative data were processed with HKL2000 (ref. 34) and the native data with d*TREK (Molecular Structure Corp.). MAD data for the Sx, Sn1Sn2, and Sn1Sn2Sx selenomethionine-labelled complexes were collected at beamline 1-5 at SSRL using a Quantum-4 CCD detector (Area Detector Systems) and were processed with DENZO/SCALEPACK[34]. All diffraction data were collected at 100 K.

Heavy-atom sites. Fifteen of the twenty-one selenium sites of the selenomethionine-labelled-Sn1 data set were found by the Patterson search method implemented in the crystallography and NMR system (CNS)[35] using the selenomethionine Sn1 diffraction data at the selenium anomalous peak wavelength. One extra site was found by peak searching using a log-likelihood gradient map[36] after MAD phasing. A Fourier difference map showed two iodine substitutions *ortho* to the hydroxyl group in Tyr 88 of Sb. Additional ordered selenomethionine sites from appropriately labelled complexes were obtained by Fourier difference maps using the Sn1Sn2 λ_3 diffraction data. This produced a total of 15 ordered sites out of 18 in Sx, 16 out of 21 in Sn1 and 15 out of 21 in Sn2.

Multi-MAD phasing. Heavy-atom parameter refinement and phasing were carried out individually for the three MAD experiments using CNS (Table 1 in Supplementary Information)[35]. MAD phasing used the Phillips–Hodgson method[37] formulated in a maximum-likelihood framework[38]. Density modification consisted of solvent flattening[39] using an envelope determined by electron-density fluctuations, histogram matching[40], and phase extension from 3 Å to 2.4 Å resolution using the native diffraction data. Several regions showed only weak or variable electron density, especially at the N-terminal end of the complex, using the individual MAD data sets. Phase combination of the three MAD-phase sets with unit weighting followed by density modification produced a significantly improved electron-density map (Table 1 in Supplementary Information, and Fig. 1). The unweighted phase differences at 50–3.0 Å resolution between the final model and the various phase sets after density modification were: 58.2° for Sx, 48.1° for Sn1Sn2, 51.2° for Sn1SnSx, 43.1° for the combination of Sx and Sn1Sn2, and 42.1° for the combination of all three MAD data sets. The experimental electron-density map showed most of the

model. Most of the remaining parts of the model became traceable in phase-combined electron density maps.

Refinement. The initial model was built using the program O (ref. 41). Refinement was carried out using torsion-angle simulated annealing[42] and conjugate gradient minimization, interspersed with restrained individual atomic thermal factor refinement[43] as implemented in CNS[35]. The MLHL maximum likelihood target[44] was used with density-modified phases as prior experimental phase information. Model quality was periodically checked using CNS[35]. Subsequent model-building stages used phase-combined σ_A-weighted electron density maps[45] using the combined phases from all three MAD experiments and the present model phases. Refinement included a uniform bulk solvent correction ($B_{sol} = 38.5$ Å^2; $k_{sol} = 0.39$ e$^-$/Å^3) and overall aniso-tropic thermal factor ($B_{11} = -1.54$ Å^2; $B_{22} = -8.86$ Å^2; $B_{33} = 10.40$ Å^2) refinement. As the three complexes exhibited significant differences, especially at their N and C termini (Fig. 2b), non-crystallographic symmetry (NCS) restrains were not applied and the complexes were build independently. At this resolution, refinement in the absence of NCS restrains can be justified as high-quality phase information was used in the refinement target function. All diffraction data were used throughout the refinement except that a 10% randomly selected test set for cross-validation σ_A values was used in the maximum likelihood calculations[47] and calculation of R_{free} (ref. 46). Strontium sites were identified by the average anomalous signal of the ion at the Sx, Sn1Sn2 and Sn1Sn2Sx low-energy-remote (λ_1) wavelengths (Table 1) and by proper divalent-cation-coordinating ligation. Water molecules were placed at sites corresponding to σ_A-weighted-difference Fourier peaks greater than 3σ that exhibited reasonable protein–solvent hydrogen-bonding distances without steric conflict. MPD molecules were also included in the structure on the basis of the overall shape and coordination of the electron density from difference Fourier and σ_A-weighted $2F_o - F_c$ maps. The final model contains residues: Sb 25–93, Sx 188–259, Sn1 7–83 and Sn2 131–204 for complex I; Sb 28–96, Sx 189–261, Sn1 12–83 and Sn2 132–203 for complex II; Sb 26–94, Sx 186–259, Sn1 11–83 and Sn2 132–204 for complex III; 19 water molecules; 13 Sr^{2+} ions; and 7 MPD molecules. The model exhibits excellent stereochem-istry and structure quality, with an average bond length and bond-angle deviation of 0.009 Å and 1.34°, respectively, no Ramachandran violations, and a B-factor r.m.s.d. for main-chain bonds of 1.38 Å^2 and for sidechain bonds of 2.4 Å^2. The overall free R-value is 30.3% and the R value is 26.5%, using all observed diffraction data between 50 and 2.4 Å resolution. No amplitude-based cutoffs were applied.

Structure analysis. Analysis of α-helical parameters (crossing angle, number of residues per turn, radius of helical bundle and layer analysis) was done for the four-helical-bundle region of the synaptic fusion complex (layers '7' to '8', (Table 2 in Supplementary Information). The crossing angles range between 15° and 25° for synaptobrevin, 5° and 20° for syntaxin, 5° and 20° for Sn1, and 12° and 25° for Sn2. The crossing angles are defined as the dihedral angle between the local helical axes and the bundle axis. The local helical axis is defined as the vector between centroids of the C α, N and C positions of two sets of seven consecutive residues spaced apart by half an α-helical turn. Surface plots and electrostatic analyses were done with GRASP[48]. Figures 1, 2a, 3 and 5 were prepared with gl_render (provided by L. Esser) or Bobscript[49], and were rendered using PovRay (http://www.povray.org/).

1. Südhof, T. The synaptic vesicle cycle: a cascade of protein–protein interactions. *Nature* **375,** 645–653 (1995).
2. Hanson, P. I., Heuser, J. E. & Jahn, R. Neurotransmitter release—four years of SNARE complexes. *Curr. Opin. Neurobiol.* **7,** 310–315 (1997).
3. Jahn, R. & Niemann, H. Molecular mechanisms of clostridial neurotoxins. *Ann. NY Acad. Sci.* **733,** 245–255 (1994).
4. Söllner, T., Bennett, M. K., Whiteheart, S. W., Scheller, R. H. & Rothman, J. E. A protein assembly-disassembly pathway *in vitro* that may correspond to sequential steps of synaptic vesicle docking, activation, and fusion. *Cell* **75,** 409–418 (1993).
5. Hayashi, T., Yamasaki, S., Nauenburg, S., Binz, T. & Niemann, H. Disassembly of the reconstituted synaptic vesicle membrane fusion complex *in vitro. EMBO J.* **14(10),** 2317–2325 (1995).
6. Fasshauer, D., Otto, H., Eliason, W. K., Jahn, R. & Brunger, A. T. Structural changes are associated with SNARE-complex formation. *J. Biol. Chem.* **242,** 28036–28041 (1997).
7. Nichols, B. J., Ungerman, C., Pelham, H. R. B., Wickner, W. T. & Haas, A. Homotypic vacuolar fusion mediated by t- and v-SNAREs. *Proc. Natl Acad. Sci. USA* **387,** 199–202 (1997).
8. Otto, H., Hanson, P. I. & Jahn, R. Assembly and disassembly of a ternary complex of synaptobrevin, syntaxin, and SNAP-25 in the membrane of synaptic vesicles. *Proc. Natl Acad. Sci. USA* **94,** 6197–6201 (1997).
9. Block, M. R., Glick, B. S., Wilcox, C. A., Wieland, F. T. & Rothman, J. E. Purification of an N-

ethylmaleimide-sensitive protein catalyzing vesicular transport. *Proc. Natl Acad. Sci. USA* **85,** 7852–7856 (1988).

10. Hanson, P. I., Otto, H., Barton, N. & Jahn, R. The N-ethylmaleimide-sensitive fusion protein and α-SNAP induce a conformational change in syntaxin. *J. Biol. Chem.* **270,** 16955–16961 (1995).

11. Fasshauer, D., Eliason, W. K., Brunger, A. T. & Jahn, R. Identification of a minimal core of the synaptic SNARE-complex sufficient for reversible assembly and disassembly. *Biochemsitry* **37,** 10345–10353 (1998).

12. Hendrickson, W. A. Determination of macromolecular structures from anomalous diffraction of synchrotron radiation. *Science* **254,** 51–58 (1991).

13. Hanson, P. I., Roth, R., Morisaki, H., Jahn, R. & Heuser, J. E. Structure and conformational changes in NSF and its membrane receptor complex visualized by quick-freeze/deep-etch electron microscopy. *Cell* **90,** 523–525 (1997).

14. Oyler, G. A. *et al.* The identification of a novel synaptosomal-associated protein, SNAP-25, differentially expressed by neuronal subpopulations. *J. Cell. Biol.* **109,** 3039–3052 (1989).

15. Harbury, P. B., Zhang, T., Kim, P. S. & Alber, T. A switch between two-, three-, and four-stranded coiled coils in GCN4 leucine zipper mutants. *Science* **262,** 1401–1407 (1993).

16. Lupas, A., van Dyke, M. & Stock, J. Predicting coiled coils from protein sequences. *Science* **252,** 1162–1164 (1991).

17. Crick, F. H. C. The packing of α-helices: simple coiled coils. *Acta Crystallogr.* **6,** 689–697 (1953).

18. Wolf, E., Kim, P. S. & Berger, B. MultiCoil: a program for predicting two- and three-stranded coiled coils. *Protein Sci.* **6,** 1179–1189 (1997).

19. Weimbs, T., Mostov, K. E., Low, S. H. & Hofmann, K. A model for structural similarity between different SNARE complexes based on sequence relationships. *Trends Cell Biol.* **8,** 260–262 (1998).

20. Hao, J. C., Salem, N., Peng, X. R., Kelly, R. B. & Bennett, M. K. Effect of mutations in vesicle-associated membrane protein (VAMP) on the assembly of multimeric protein complexes. *J. Neurosci.* **17,** 1596–1603 (1997).

21. Saifee, O., Wei, L. & Nonet, M. L. The *Caenorhabditis elegans* unc-64 locus encodes a syntaxin that interacts genetically with synaptobrevin. *Mol. Biol. Cell* **9,** 1235–1239 (1998).

22. Fasshauer, D., Bruns, D., Shen, B., Jahn, R. & Brunger, A. T. A structural change occurs upon binding of syntaxin to SNAP-25. *J. Biol. Chem.* **272,** 4582–4590 (1997).

23. Kee, Y., Lin, R. C., Hsu, S. C. & Scheller, R. H. Distinct domains of syntaxin are required for synaptic vesicle fusion complex formation and dissociation. *Neuron* **14,** 991–998 (1995).

24. Hayashi, T. *et al.* Synaptic vesicle membrane fusion complex: action of clostridial neurotoxins on assembly. *EMBO J.* **13,** 5051–5061 (1994).

25. Wimley, W. C. & White, S. H. Experimentally determined hydrophobicity scale for proteins at membrane interfaces. *Nature Struct. Biol.* **3,** 842–848 (1996).

26. Chan, D. c., Fass, D., Berger, J. M. & Kim, P. S. Core structure of gp41 from the HIV envelope glycoprotein. *Cell* **89,** 263–273 (1997).

27. Weissenhorn, W., Dessen, A., Harrison, S. C., Skehel, J. J. & Wiley, D. C. Atomic structure of the ectodomain from HIV-1 gp41. *Nature* **387,** 426–430 (1997).

28. Caffrey, M. *et al.* Three-dimensional solution structure of the 44 kDa ectodomain of SIV gp41. *EMBO J.* **17,** 4572–4584 (1998).

29. Wilson, I. A., Skehel, J. J. & Wiley, D. C. Structure of the haemagglutinin membrane glycoprotein influenza virus at 3 Å resolution. *Nature* **289,** 366–373 (1981).

30. Rice, L. M., Brennwald, P. & Brunger, A. T. Formation of a yeast SNARE complex is accompanied by significant structural changes. *FEBS Lett.* **415,** 49–55 (1997).

31. Chan, D. C. & Kim, P. S. HIV entry and its inhibition. *Cell* **93,** 681–684 (1998).

32. Bernard, A. & Payton, M. Fermentation and growth of *Escherichia coli* for optimal protein production. *Curr. Protocol. Protein Sci.* **5.3,** 1–18 (1995).

33. Leahy, D. J., Erickson, H. P., Aukhil, I., Joshi, P. & Hendrickson, W. A. Crystallization of a fragment of human fibronectin: introduction of methionine by site-directed mutagenesis to allow phasing via selenomethionine. *Proteins* **19,** 48–54 (1994).

34. Otwinowski, Z. & Minor, W. Processing of X-ray diffraction data collected in oscillation mode. *Methods Enzymol.* **276,** 307–326 (1998).

35. Brunger, A. T. *et al.* Crystallography & NMR system (CNS): a new software system for macromolecular structure determination. *Acta Crystallogr. D* **54,** 905–921 (1998).

36. Bricogne, G. Bayesian statistical viewpoint on structure determination: basic concepts and examples. *Methods Enzymol.* **276,** 361–423 (1997).

37. Phillips, J. C. & Hodgson, K. O. The use of anomalous scattering effects to phase diffraction patterns from macromolecules. *Acta Crystallogr. A* **36,** 856–864 (1980).

38. Burling, F. T., Weis, W. I., Flaherty, K. M. & Brunger, A. T. Direct observation of protein solvation and discrete disorder with experimental crystallographic phases. *Science* **271,** 72–77 (1996).

39. Wang, B.-C. Resolution of phase ambiguity in macromolecular crystallography. *Methods Enzymol.* **115,** 90–112 (1985).

40. Zhang, K. Y. J. & Main, P. Histogram matching as a new density modification technique for phase refinement and extension of protein molecules. *Acta Crystallogr. A* **46,** 41–46 (1990).

41. Jones, T. A., Zou, J. Y., Cowan, S. & Kjeldgaard, M. Improved methods for building protein models in electron density maps and the location of errors in these models. *Acta Crystallogr. A* **47,** 110–119 (1991).

42. Rice, L. M. & Brunger, A. T. Torsion angle dynamics: reduced variable conformational sampling enhances crystallographic structure refinement. *Proteins* **19,** 277–290 (1994).

43. Hendrickson, W. A. Stereochemically restrained refinement of macromolecular structures. *Methods Enzymol.* **115,** 252–270 (1985).

44. Pannu, N. S., Murshudov, G. N., Dodson, E. J. & Read, R. J. Incorporation of prior phase information strengthens maximum likelihood structural refinement. *Acta Crystallogr. D* (in the press).

45. Read, R. J. Improved Fourier coefficients for maps using phases from partial structures with errors. *Acta Crystallogr. A* **42,** 140–149 (1986).

46. Brunger, A. T. The free *R* value: a novel statistical quantity for assessing the accuracy of crystal structures. *Nature* **355,** 472–474 (1992).

47. Read, R. J. Model phases: probabilities and bias. *Methods Enzymol.* **277,** 110–128 (1997).

48. Nicholls, A., Sharp, K. A. & Honig, B. Protein folding and association: insights from the interfacial and thermodynamic properties of hydrocarbons. *Proteins* **11,** 281–296 (1991).

49. Esnouf, M. An extensively modified version of MOLSCRIPT that includes greatly enhanced coloring capabilities. *J. Mol. Graph. Model* **15,** 132–134 (1997).

50. Jorgensen, W. L. & Rives, J. T. The OPLS potential functions for protein energy minimizations for crystals of cyclic peptide and crambin. *J. Am. Chem. Soc.* **110,** 1657–1666 (1988).

51. Malashkevich, V. N., Chan, D. C., Chutkowski, C. T. & Kim, P. Crystal structure of the simian immunodeficiency virus (SIV) gp41 core: Conserved helical interactions underlie the broad inhibitory activity of gp41 peptides. *Proc. Natl Acad. Sci. USA* **95,** 9134–9139 (1998).